Opto-Electronic Advances

Review

2019, Vol. 2, No. 10

DOI: 10.29026/oea.2019.190023

Recent improvement of silicon absorption in opto-electric devices

Takashi Yatsui

Silicon dominates the contemporary electronic industry. However, being an indirect band-gap material, it is a poor absorber of light, which decreases the efficiency of Si-based photodetectors and photovoltaic devices. This review highlights recent studies performed towards improving the optical absorption of Si. A summary of recent theoretical approaches based on the first principle calculation has been provided. It is followed by an overview of recent experimental approaches including scattering, plasmon, hot electron, and near-field effects. The article concludes with a perspective on the future research direction of Si-based photodetectors and photovoltaic devices.

Keywords: Si; indirect band gap; plasmon; first principle calculation; near-field effect

Yatsui T. Recent improvement of silicon absorption in opto-electric devices. *Opto-Electron Adv* **2**, 190023 (2019).

Introduction

Si is an integral part of all electronic devices. It plays an important role in opto-electronic devices such as photodetectors and photovoltaic devices[1,2]. However, since it is an indirect band-gap material, phonon assistance is required in the photo-excitation process to compensate the wave-vector difference between the valence band maximum and the conduction band minimum of holes (Γ point) and electrons (X point), respectively (Fig. 1[3]). Therefore, although Si dominates the photonics devices, a field that is better known as Si photonics[4], it is a substrate for the light emitting materials[5,6]. Moreover, it can be used for a much wider variety of applications if its optical absorption in the telecommunication wavelength range is improved[7]. In this article, some important recent studies directed towards improving the performance of Si photonic devices have been reviewed.

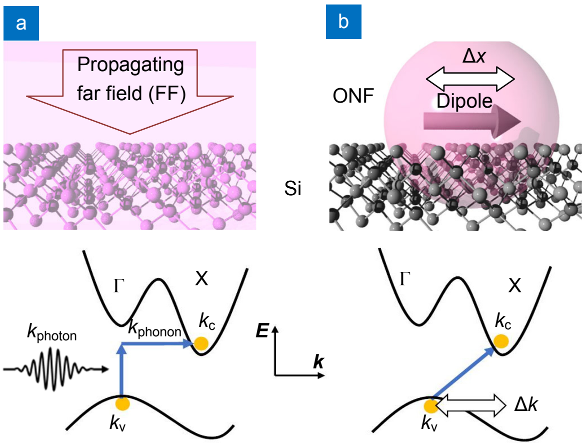

Fig. 1 | Comparison of far- and near-field excitations. (**a**) Far-field (FF) excitation of Si. Here k_{photon}, k_c, k_v, and k_{phonon} are the wave vectors of photon, conduction band, valence band, and phonon, respectively. (**b**) Optical near-field (ONF) excitation of Si. Figure is reproduced from ref.[3] under the terms of the Creative Commons Attribution 4.0 International license.

Theoretical advances

Optical near-field (ONF) effect can potentially improve the carrier excitation in indirect band-gap materials. This is attributed to the fact that ONF is expected to have large wave vector components (Δk), which implies very small Δx, due to the field localization. This was validated in a study which demonstrated that ONFs, as a dipole-mode plasmon, generate carriers directly[8]. It was shown that in small particles, the plasmons induce an electric field that exhibits Fourier components with large wave numbers. Furthermore, it was demonstrated that such an electric field generates carriers without phonon assistance. Further investigation of the ONF excitation was performed

School of Engineering, University of Tokyo, Tokyo 113-8656, Japan.
*Correspondence: T Yatsui, E-mail: yatsui@lux.t.u-tokyo.ac.jp

Received: 10 June 2019; Accepted: 29 August 2019; Published: 18 October 2019

in a system comprising of metallic nanospheres embedded in crystalline Si[9]. Here, the excitation was evaluated under the framework of linear perturbation theory, and it was found that the ONF effect is too weak to be measured in a real system. However, these calculations were based on analytical model systems, and not on the real carrier excitations.

To this end, Yamaguchi et al.[10] evaluated the carrier dynamics using first-principles calculations, where they calculated the electron excitation by considering the indirect interband transition between states with different Bloch wave numbers. Instead of using the Bloch condition, which cannot describe the indirect interband transitions, they implemented the Born-von Kármán boundary condition[11,12]. Further, they also performed a time-dependent calculation of the ONF excitation using one-dimensional Kronig-Penny (1D-KP) model (Figs. 2(a) and 2(b)). They considered the dispersion relation with an indirect band gap (Fig. 2(c)). As shown in Figs. 2(d) and 2(e), it was observed that the absorption spectra for far-field excitation decreases at the band-gap energy (E_d), while the absorption spectrum for near-field excitation decreases at the band-gap energy (E_g) (much smaller than E_d) which was realized by the direct excitation. Furthermore, they clearly showed that the near-field component of the dipole radiation (r^{-3}) is the origin of ONF excitation[13].

A more detailed investigation of the ONF excitation in realistic three dimensional Si systems (Fig. 3(a)) was reported recently[14]. Here, a real-time and real-space grid-based time-dependent density-functional theory (DFT) approach[15–17] was used. A supercell method along with the Born-von Kármán periodic condition was implemented to calculate the wave-vector excitation[11], where the vertical band gap energy at the Γ point was 2.0 eV. In this system, the source of the ONF was a y-polarized point dipole with the near-field component (r^{-3}), which was set 5 Å apart from the surface of Si. Thus, realistic metallic structures, which could generate plasmon, were not treated explicitly in this study. The potentials of the ONF were described by

$$V_{\mathrm{near}}(r,t)=-\frac{C(y-y_{\mathrm{p}})}{r^3}\sin(\omega t)\sin^2(\frac{\pi t}{T}) \quad , \qquad (1)$$

where ω is the frequency of the oscillating dipole, C is a constant, and T = 30 fs is the pulse duration. The electric field distribution induced by the oscillating dipole, as described by Eq. (1) is non-uniform in spatial domain (see Fig. 3(b)). Therefore, it results in the generation of large components of the Fourier domain as shown in Fig. 3(c), which implies that the ONF has large wave vectors. Based on these observations, the absorption intensity was obtained by calculating the transition probability. As shown in Fig. 3(d), the absorption intensity for the far-field excitation (blue solids circles and blue line) decreases around 2.0 eV, which corresponds to the band gap energy at the Γ point. On the contrary, the ONF induces a sufficiently large absorption intensity, which causes a red shift of the absorption spectra (red solid circles and red line in Fig. 3(d)). Furthermore, direct optical transitions between different wave vectors were also confirmed. Figure 3(e) shows the absorption intensity as a function of the variation in wave vector for the electronic excitation between second-highest valence band and the lowest conduction band in the ONF excitation at 1.6 eV. Here, the absorption intensity is maximum at Δk ~4 nm^{-1}.

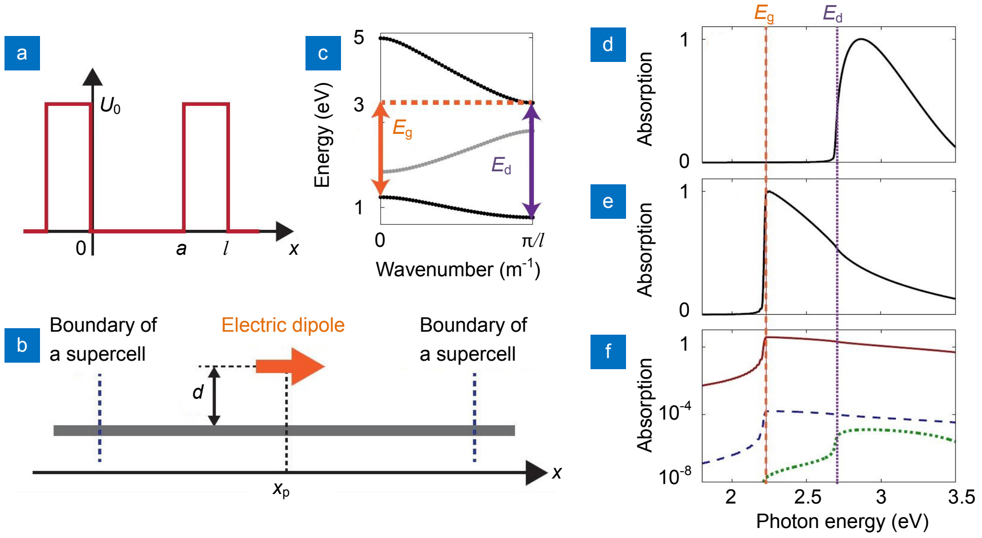

Fig. 2 | ONF excitation in indirect band-gap structure. (**a**) Potential, (**b**) a schematic of the 1D-KP model, and (**c**) dispersion relation. Here, E_g: band-gap energy and E_d: direct band-gap energy. Frames (**d**) and (**e**) show the normalized absorption spectra of the 1D-KP model due to the far- and near-field excitations, respectively. (**f**) Absorption spectra due to the electric field components from the dipole radiation, which are r^{-3} (red solid line), r^{-2} (blue dashed line), and r^{-1} (green dotted line). Figure is reprinted with permission from ref.[10], Copyright © 2016 American Physical Society.

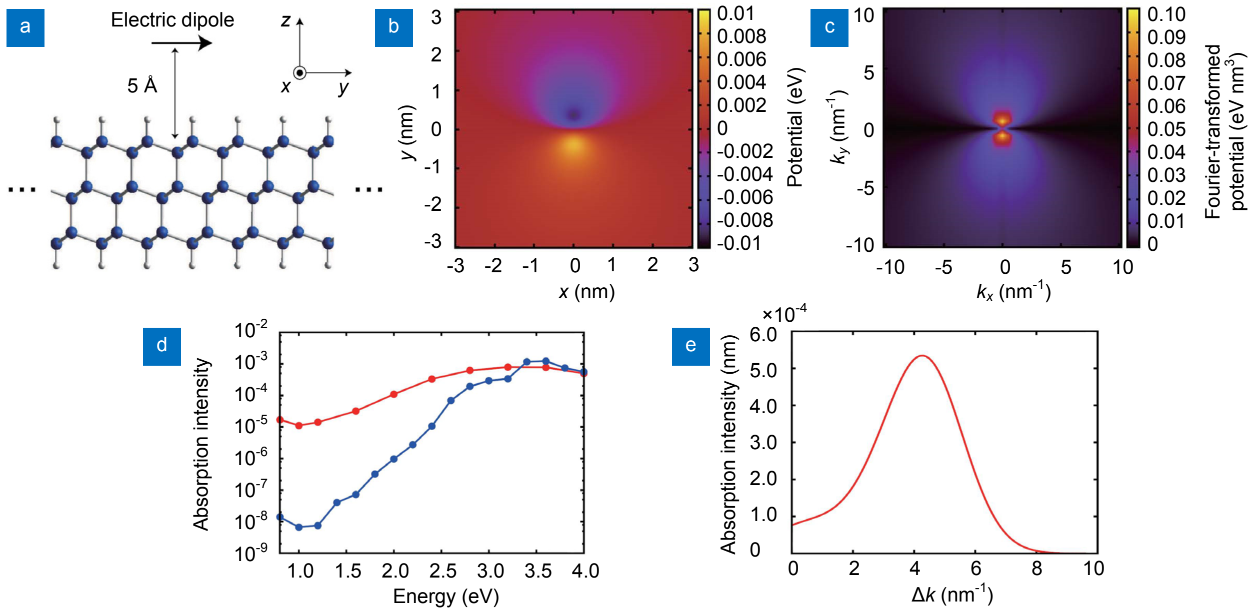

Fig. 3 | ONF excitation in a realistic Si system. (**a**) The theoretical model consisting of a Si bilayer and the electric dipole measured at a distance of 5 Å above Si surface. (**b**) Potential of the ONF induced by the electric dipole shown in (a). (**c**) The Fourier transform of (b). (**d**) Comparison of the absorption intensity for far-field (blue) and near-field (red) excitations. (**e**) Absorption intensity as a function of the variation in the wave vector (Δk) for the excitation at 1.6 eV. Figure is reproduced from ref.[14] under the terms of the Creative Commons Attribution 4.0 International license.

This was the direct evidence of the wave-vector excitation induced by the ONF. In other words, the direct ONF excitation does not require phonon assistance and can be realized with photons exclusively.

Experimental advances

Scattering effect: Black Si

A simple yet effective way to improve the optical absorption in the solar cells is to increase the optical path length through the depletion layer between the p-n junction. To improve the light scattering efficiency, the scatterers have been fabricated at the surface of the detector, such as pyramidal Si hillocks made by the anisotropic etching[18], vertically aligned single crystalline Si nanowire array[19], or needles made by the laser irradiation with the ultra-short pulse width[20]. In particular, the latter (Si surface with needles) works as an extremely good scatterer because of its small sharp tip with no reflection from the surface. Consequently, it appears black, and is therefore called a black Si. This black Si has been used to develop highly efficient Si solar cells with 22.1% efficiency[21,22].

Plasmonic effect

To improve the scattering efficiency, many researchers utilized the field enhancement using the plasmon resonance[23,24]. The scattering and absorption cross-sections are given by point dipole model[25]:

$$C_{\text{sca}} = \frac{k^4}{6\pi}|\alpha|^2 = \frac{8\pi}{3}\left(\frac{2\pi}{\lambda}\right)^4 a^6 \left|\frac{\varepsilon-\varepsilon_{\text{m}}}{\varepsilon+2\varepsilon_{\text{m}}}\right|^2 , \tag{2}$$

$$C_{\text{abs}} = k\,\text{Im}[\alpha] = 4\pi\left(\frac{2\pi}{\lambda}\right)a^3\left[\frac{\varepsilon-\varepsilon_{\text{m}}}{\varepsilon+2\varepsilon_{\text{m}}}\right] , \tag{3}$$

where α is the polarizability, a is the radius of the particle, ε is the dielectric function of the particle, ε_{m} is the dielectric function of the surrounding media, and λ is the wavelength. It is evident from Eq. (2) that ε should be negative ($-2\varepsilon_{\text{m}}$), i.e., the scatterer should be a metal, to utilize the plasmon resonance for the light scattering. Further from Eq. (3), it is clear that the plasmon induced light scattering is indispensable for a strong optical absorption. For a more effective trapping of the scattered light at the metallic nanoparticles on the surface, the scattered light excites the waveguide mode using a thin Si substrate of Si-on-insulator (SOI)[26,27] wafer. Furthermore, a higher coupling efficiency can be realized by controlling the size and the shape of the metallic nanoparticle[28,29]. In particular, it was observed that smaller size, as well as cylindrical and hemispherical shapes of spheres lead to a longer path length in the substrate. Further improvement of the carrier-excitation was realized by introducing a photonic design to induce light trapping with three-dimensional structures consisting of nanowires and nanoparticles[30,31]. Since the plasmon resonance for the Au sphere occurs at ~520 nm, ellipsoid shape[32], chains of nanoparticles[33], or elongated shapes such as nanorod[34] with longer resonance wavelength have been implemented to obtain larger absorbance in this wavelength range. In addition, the periodic structure of the metal, i.e., metamaterial-plasmonic absorbers[35,36], has been investigated to enhance the optical absorption. The periodic structure works as a grating coupler of light with a normal incident angle. Consequently, it results in a strong absorption exceeding 80%. We investigated the self-assembly method[37] to improve the efficiency of nanoparticles deposition. Using the laser-assisted deposition of the electrode metal with a reverse biased p–n junction, we realized a selective photocurrent generation in the transparent wavelength range[38]. We observed a drastic change in the surface morphology of the metal, and confirmed the increase in the photocurrent at the wavelength that is close to that used during the electrode deposition. Since Au has high absorption coefficient, alternative materials, such as transparent conducting oxides were considered to achieve the resonance at longer wavelengths[39,40].

Hot electrons

The internal photoemission on a Schottky barrier (Fig. 4) has been investigated to utilize the scenarios where the photon energy is lower than the band gap energy of Si (E_C–E_V = 1.1 eV)[41–43]. Since the Schottky barrier between Au and Si (ϕ_B ~ 0.5 eV) is lower than the band gap energy of Si, the infrared wavelength region that is longer than the band-gap wavelength (1100 nm) can be used. The carriers of electron (hot electrons) were excited to obtain energies that are higher than the Schottky barrier. By optimizing the plasmon resonator, the responsivity of 4.5×10^{-4} A W^{-1} was obtained at nearly 1600 nm (~0.77 eV). Using a three dimensional plasmonic resonator, a photocapacitance structure was developed to detect the charge generation at the Schottky barrier with higher efficiency (Fig. 4(b))[44].

Near-field effect

As discussed in the previous section, the ONF effect can improve the absorption efficiency at the band-gap wavelength. This implies that the localized field can induce large wave vector components, which in turn leads to direct excitation in indirect band-gap semiconductors (Fig. 1(b)). To corroborate this effect, we fabricated a Si photodetector with a lateral p–n junction (Fig. 5(a))[3]. We avoided the field enhancement due to the Au nanoparticles[24,26,27] in this device by introducing their near-field sources with extremely low coverage ~2 % (Figs. 5(b) and 5(c)). Consequently, we observed a 40 % increase in the photosensitivity as compared to that without Au nanoparticles (Figs. 5(d) and 5(e)). As shown in Fig. 5(e), the photosensitivity rate increased at longer wavelengths near the band-gap wavelength. This dependence has not been reported for devices that utilized plasmon resonance[23,24,26,27], where the enhancement in photosensitivity exhibits a peak around the plasmon resonance, which is determined by the materials and shapes. To find the origin of this dependence, we evaluated the wavelength dependence under the assumption that the ONF effect causes a direct excitation in the indirect band-gap semiconductor. The absorption coefficients of the indirect (α_I) and the direct (α_D) band-gap materials near the energy band gap E_g are described as[45]

$$\alpha_I \propto (h\nu - E_g)^2 / h\nu \quad , \tag{4}$$

$$\alpha_D \propto (h\nu - E_g)^{1/2} / h\nu \quad , \tag{5}$$

where h is Planck constant and ν is frequency of light. Since the bias voltage was 0, the photo-current becomes the short circuit current described as[46]

$$I_{SC} = Q(1-R)\{1-\exp(-\alpha l)\}en \quad , \tag{6}$$

where Q is the collection efficiency, R is the reflection coefficient, l is the absorbing layer thickness, e is the electron charge, and n is the number of photons per second per unit of the p–n junction. The ONF can induce a direct transition by the inclusion of Au nanoparticles. Thus, the photocurrent for this device is the same as that of the direct transition (I_{SC_D}). However, since the coverage of the Au nanoparticles A is not 100 %, the photocurrent shows an increase in the regions where Au nanoparticles existed (the ratio was A), while it remained the same (the ratio was (1-A)) in other regions. Thus, the increased rate in the device can be expressed as follows:

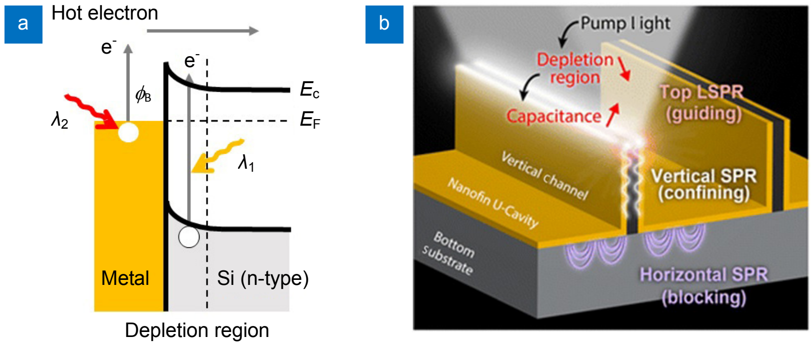

Fig. 4 | Schematic of the hot electron driven photocurrent over a Schottky barrier. (**a**) The Schottky barrier (ϕ_B) is lower than the band-gap energy. Therefore, a longer wavelength (λ_2) can be utilized instead of the band-gap wavelength (λ_1). Here, E_C: conduction band energy, E_V: valence band energy, and E_F: Fermi level energy. (**b**) Three dimensional plasmonic photocapacitor structure. Figure (b) is reprinted with permission from ref.[44], Copyright © 2016 American Chemical Society.

$$\begin{aligned}&\frac{AI_{\mathrm{SC\_D}}+(1-A)I_{\mathrm{SC\_I}}}{I_{\mathrm{SC\_I}}}\\&=\frac{A\big(1-\exp(-\alpha_{\mathrm{D}}l)\big)+(1-A)\big(1-\exp(-\alpha_{\mathrm{I}}l)\big)}{1-\exp(-\alpha_{\mathrm{I}}l)}\\&\approx\frac{\big(A\alpha_{\mathrm{D}}+(1-A)\alpha_{\mathrm{I}}\big)l}{\alpha_{\mathrm{I}}l}\\&=C\frac{A(h\nu-E_{\mathrm{g}})^{1/2}+(1-A)(h\nu-E_{\mathrm{g}})^{2}}{(h\nu-E_{\mathrm{g}})^{2}}\quad,\qquad(7)\end{aligned}$$

where C is the proportional constant. As shown in Fig. 5(e), the solid curves represent the calculated increased rates, where blue, red, and black curves correspond to N = 10, 5, and 1, respectively. The experimental data confirmed that the observation of increased rate near the band-gap energy supports the possibility of the direct transition by the ONF. Further improvement of the increased rate can be realized by implementing a larger coverage of the Au nanoparticles and a larger depletion area by introducing the intrinsic Si layer between the p- and n-type layers, i.e., p–i–n diode structure.

Figure 6(a) shows the variation of increased rate as a function of size of the Au nanoparticles. We observe that the increased rate is maximum for Au nanoparticle with a diameter of 100 nm. To quantify this size dependence, numerical calculations were performed using a finite difference time domain (FDTD) method[47]. The calculated field distributions (Fig. 6(b)) were then used to obtain the Fourier spectra (Fig. 6(c)), where the spectra were obtained from the cross-sectional profile of the field distribution along the x-axis and they were averaged along y-axis $0 \le y \le D/2$ (D is the diameter of Au nanoparticle). Since the wave number difference between the Γ and X points ($k_{x\_\Gamma\mathrm{X}}$) is 4.92 nm^{-1} [48], we studied the diameter dependence of the power spectrum at $k_{x\_\Gamma\mathrm{X}}$ ($|F(E)_{\Gamma\mathrm{X}}|^2$, red circles in Fig. 6(d)). It is observed that $F(E)_{\Gamma\mathrm{X}}|^2$ also attains a maximum at D = 100 nm. The calculated size dependence is found to be in good agreement with the experimental results (Fig. 6(a)). The effect of generating a larger k-component by the ONF was then investigated by determining the normalized power spectra. This normalization was performed using the square of the volume of Au nanoparticles (open blue circles in Fig. 6(d))[49]. The normalized power spectra increase with a decrease in size. These calculations confirm that, a greater Δk is generated when the size of Au nanoparticles decreases. In other words, the efficiency of the direct optical transition by the ONF increases with a decrease in size due to large components of the wave number.

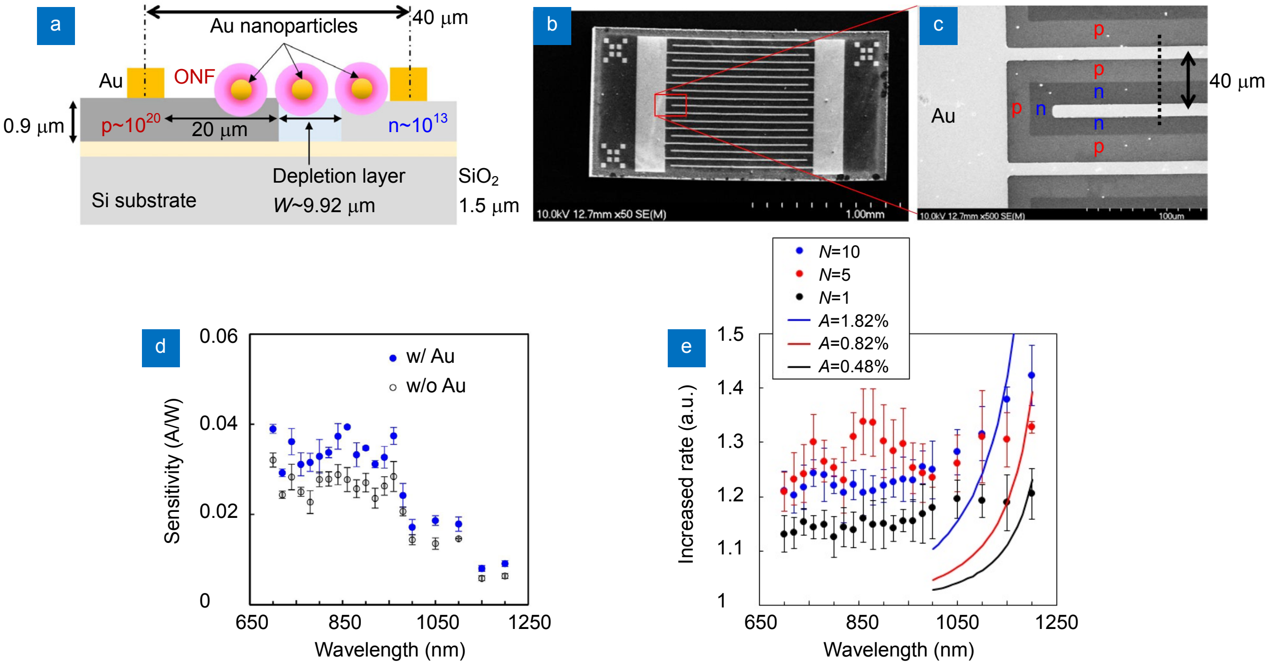

Fig. 5 | Sensitivity of the lateral p–n junction with Au nanoparticles. (**a**) Schematic of the device using a Si-on-insulator (SOI). As described in ref.[3], a solution containing Au nanoparticles was dispersed on the device and the solvent was evaporated with a hot plate. We counted this procedure of the dispersion number N as one. (**b**) Scanning electron micrographic (SEM) image of the device. (**c**) Magnified SEM image of (b). (**d**) Wavelength dependence of sensitivity of the devices. The solid blue circles show the device with the 100-nm Au nanoparticles (N = 5). The open black circles correspond to the device before the Au nanoparticle dispersion. (**e**) Increased photosensitivity rate as a function of the excitation wavelength with different dispersion number N. Increased rate were obtained as the ratio between the photosensitivity of the device with and without Au nanoparticles. The solid curves show the calculated increased rate using Eq. (7). We used the Au nanoparticle coverage determined by SEM images as the ratios of the direct transition A: A=1.82% (N=10), 0.82% (N=5), and 0.48% (N=1). Figure is reproduced from ref.[3] under the terms of the Creative Commons Attribution 4.0 International license.

Although the theoretical results of the large Δk generated using the first-principle calculation[14] supported the experimental results[3] qualitatively, the enhancement value was not explained quantitatively. The disagreement might be due to the disagreement of the materials and the size. For example, in the first-principle calculation, the point dipole was used as a source of the ONF. More detailed calculations using the real material in a real system will be required to discuss quantitatively. In addition, the limitation of the material size in the first-principle calculation results in the disagreement of the system size. To resolve this disagreement, a smaller size of the source for ONF generation should be used, such as porous Si with several nanometer scale[50–52].

Summary and future directions

Si is an indirect band-gap semiconductor and therefore exhibits poor optical absorption efficiency. This review presents an overview of various theoretical and experimental efforts to improve the performance of Si-based photodetectors and photovoltaic devices. The theoretical framework based on first principle calculations along with experiments including scattering effect, plasmon effect, hot electrons, and near-field effect were discussed. The ONF effect permits the generation of a large Δk by field localization, which in turn can improve the absorption efficiency of these devices. The ONF effect can intrinsically induce a direct transition due to nonuniformity of the optical field. In addition to the reviewed topics, we confirmed that near-field could enhance the optical absorption by the field enhancement effect[53], which does not utilize plasmon resonance. The field enhancement by ONF was confirmed both in the first-principle calculation and in the experimental absorption spectra of the metal complex for CO_2 reduction. Therefore, if the near-field source is placed with appropriate position, further enhancement of absorption is expected. Further, since the ONF has nonuniform optical field distribution in nanoscale, the ONF can generate even harmonics in materials with inversion symmetry[54]. Yamaguchi et al. have showed that the ONF inherently realizes strong second harmonic generation (SHG) and suggested ways to improve the efficiency of this process[16,55–57]. Further improvements of Si-based opto-electronic devices may be achieved by combining and optimizing these effects. Recently, the band engineering method was proposed to enhance the absorption in another indirect band-gap material (Ge)[58]. Similar investigations have been made in other indirect band-gap materials including InSe[59–61] and MoS_2[62,63]. The enhancement was achieved by introducing

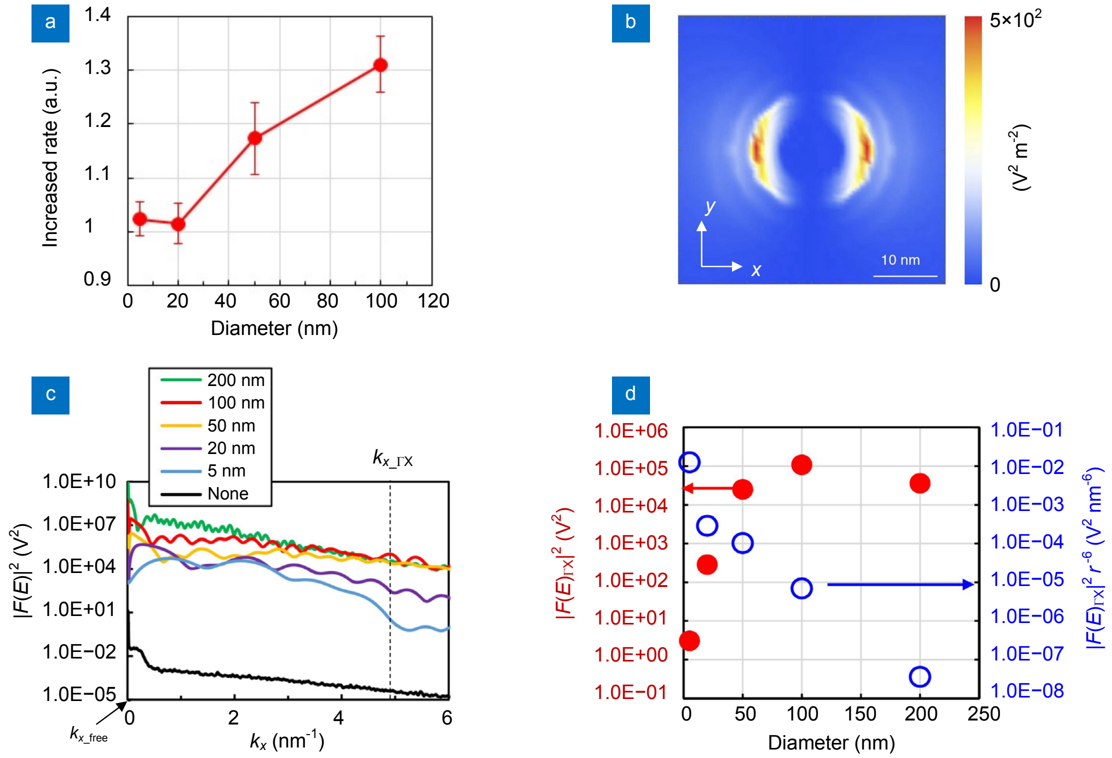

Fig. 6 | Increased rate as a function of the size of Au nanoparticles. (**a**) Increased photosensitivity rate at a wavelength of 1100 nm versus diameter of the Au nanoparticles. (**b**) Electric-field intensity distribution E^2 at the interface of Au nanoparticle (diameter D=100 nm). (**c**) Averaged ($0 \le y \le D/2$) Fourier spectra along x-axis of the electric-field. The wave number difference between the Γ and X points: $k_{x\_\Gamma X}$=4.92 nm^{-1}. (**d**) Red solid circles: the diameter dependence of the power spectra at $k_{x\_\Gamma X}$= 4.92 (nm^{-1}), $|F(E)_{\Gamma X}|^2$. Blue open circles: the normalized value of the $|F(E)_{\Gamma X}|^2$ by the square of the volume, $|F(E)_{\Gamma X}|^2 r^{-6}$. Figure is reproduced from ref.[3] under the terms of the Creative Commons Attribution 4.0 International license.

a strain in the crystal, which changed the band diagram to the direct band-gap structure. Overall, indirect bandgap materials open new avenues for various applications, which are not limited to photodetectors[64,65,66] and photovoltaic devices[1,2,] but also include other realms such as light-emitting devices[67,68], water-splitting[62,69], etc.

References

1. Green M A, Emery K, Hishikawa Y, Warta W, Dunlop E D. Solar cell efficiency tables (Version 45). *Prog Photovoltaics: Res Appl* **23**, 1–9 (2015).
2. Battaglia C, Cuevas A, De Wolf S. High-efficiency crystalline silicon solar cells: status and perspectives. *Energy Environ Sci* **9**, 1552–1576 (2016).
3. Yatsui T, Okada S, Takemori T, Sato T, Saichi K *et al.* Enhanced photo-sensitivity in a Si photodetector using a near-field assisted excitation. *Commun Phys* **2**, 62 (2019).
4. Soref R. The past, present, and future of silicon photonics. *IEEE J Sel Top Quantum Electron* **12**, 1678–1687 (2006).
5. Asghari M, Krishnamoorthy A V. Energy-efficient communication. *Nat Photonics* **5**, 268–270 (2011).
6. Wirths S, Geiger R, von den Driesch N, Mussler G, Stoica T *et al.* Lasing in direct-bandgap GeSn alloy grown on Si. *Nat Photonics* **9**, 88–92 (2015).
7. Romagnoli M, Sorianello V, Midrio M, Koppens F H L, Huyghebaert C *et al.* Graphene-based integrated photonics for next-generation datacom and telecom. *Nat Rev Mater* **3**, 392–414 (2018).
8. Kirkengen M, Bergli J, Galperin Y M. Direct generation of charge carriers in c-Si solar cells due to embedded nanoparticles. *J Appl Phys* **102**, 093713 (2007).
9. Jung J, Trolle M L, Pedersen K, Pedersen T G. Indirect near-field absorption mediated by localized surface plasmons. *Phys Rev B* **84**, 165447 (2011).
10. Yamaguchi M, Nobusada K. Indirect interband transition induced by optical near fields with large wave numbers. *Phys Rev B* **93**, 195111 (2016).
11. Martin R M. *Electronic Structure: Basic Theory and Practical Methods* (Cambridge University Press, Cambridge, 2004).
12. Ashcroft N W, Mermin N D. *Solid State Physics* (Hold, Rinehart, and Winston, New York, 1976).
13. Jackson J D. *Classical Electrodynamics* (Wiley, New York, 1962).
14. Noda M, Iida K, Yamaguchi M, Yatsui T, Nobusada K. Direct wave-vector excitation in an indirect-band-gap semiconductor of silicon with an optical near-field. *Phys Rev Appl* **11**, 044053 (2019).
15. Noda M, Ishimura K, Nobusada K, Yabana K, Boku T. Massively-parallel electron dynamics calculations in real-time and real-space: Toward applications to nanostructures of more than ten-nanometers in size. *J Comput Phys* **265**, 145–155 (2014).
16. Noda M, Yamaguchi M, Nobusada K. Second harmonic excitation of acetylene by the optical near field generated in a porous material. *J Phys Chem C* **121**, 11687–11692 (2017).
17. Iida K, Noda M, Nobusada K. Development of theoretical approach for describing electronic properties of hetero-interface systems under applied bias voltage. *J Chem Phys* **146**, 084706 (2017).
18. Baker-Finch S C, McIntosh K R. Reflection distributions of textured monocrystalline silicon: implications for silicon solar cells. *Prog Photovoltaics: Res Appl* **21**, 960–971 (2013).
19. Peng K Q, Xu Y, Wu Y, Yan Y J, Lee S T *et al.* Aligned single-crystalline si nanowire arrays for photovoltaic applications. *Small* **1**, 1062–1067 (2005).
20. Shen M Y, Crouch C H, Carey J E, Mazur E. Femtosecond laser-induced formation of submicrometer spikes on silicon in water. *Appl Phys Lett* **85**, 5694–5696 (2004).
21. Sarnet T, Carey J E, Mazur E. From black silicon to photovoltaic cells, using short pulse lasers. *AIP Conf Proc* **1464**, 219–228 (2012).
22. Savin H, Repo P, von Gastrow G, Ortega P, Calle E *et al.* Black silicon solar cells with interdigitated back-contacts achieve 22.1% efficiency. *Nat Nanotechnol* **10**, 624–628 (2015).
23. Schaadt D M, Feng B, Yu E T. Enhanced semiconductor optical absorption via surface plasmon excitation in metal nanoparticles. *Appl Phys Lett* **86**, 063106 (2005).
24. Nakayama K, Tanabe K, Atwater H A. Plasmonic nanoparticle enhanced light absorption in GaAs solar cells. *Appl Phys Lett* **93**, 121904 (2008).
25. Bohren C F, Huffman D R. *Absorption and Scattering of Light by Small Particles* (Wiley, New York, 1998).
26. Stuart H R, Hall D G. Absorption enhancement in silicon‐on‐insulator waveguides using metal island films. *Appl Phys Lett* **69**, 2327–2329 (1996).
27. Pillai S, Catchpole K R, Trupke T, Green M A. Surface plasmon enhanced silicon solar cells. *J Appl Phys* **101**, 093105 (2007).
28. Catchpole K R, Polman A. Design principles for particle plasmon enhanced solar cells. *Appl Phys Lett* **93**, 191113 (2008).
29. Catchpole K R, Polman A. Plasmonic solar cells. *Opt Express* **16**, 21793–21800 (2008).
30. Kelzenberg M D, Boettcher S W, Petykiewicz J A, Turner-Evans D B, Putnam M C *et al.* Enhanced absorption and carrier collection in Si wire arrays for photovoltaic applications. *Nat Mater* **9**, 239–244 (2010).
31. Kelzenberg M D, Turner-Evans D B, Putnam M C, Boettcher S W, Briggs R M *et al.* High-performance Si microwire photovoltaics. *Energy Environ Sci* **4**, 866–871 (2011).
32. Grand J, Adam P M, Grimault A S, Vial A, de la Chapelle M L *et al.* Optical extinction spectroscopy of oblate, prolate and ellipsoid shaped gold nanoparticles: experiments and theory. *Plasmonics* **1**, 135–140 (2006).
33. Wei Q H, Su K H, Durant S, Zhang X. Plasmon resonance of finite one-dimensional Au nanoparticle chains. *Nano Lett* **4**, 1067–1071 (2004).
34. Fan P Y, Chettiar U K, Cao L Y, Afshinmanesh F, Engheta N *et al.* An invisible metal–semiconductor photodetector. *Nat Photonics* **6**, 380–385 (2012).
35. Wang Y, Sun T Y, Paudel T, Zhang Y, Ren Z F *et al.* Metamaterial-plasmonic absorber structure for high efficiency amorphous silicon solar cells. *Nano Lett* **12**, 440–445 (2012).
36. Esfandyarpour M, Garnett E C, Cui Y, McGehee M D, Brongersma M L. Metamaterial mirrors in optoelectronic devices. *Nat Nanotechnol* **9**, 542–547 (2014).
37. Yatsui T, Nomura W, Ohtsu M. Self-assembly of size- and position-controlled ultralong nanodot chains using near-field optical desorption. *Nano Lett* **5**, 2548–2551 (2005).
38. Yukutake S, Kawazoe T, Yatsui T, Nomura W, Kitamura K *et al.* Selective photocurrent generation in the transparent wavelength range of a semiconductor photovoltaic device using a phonon-assisted optical near-field process. *Appl Phys B* **99**, 415–422 (2010).

39. Naik G V, Shalaev V M, Boltasseva A. alternative plasmonic materials: beyond gold and silver. *Adv Mater* **25**, 3264–3294 (2013).
40. Matsui H, Badalawa W, Hasebe T, Furuta S, Nomura W *et al.* Coupling of Er light emissions to plasmon modes on In_2O_3: Sn nanoparticle sheets in the near-infrared range. *Appl Phys Lett* **105**, 041903 (2014).
41. Goykhman I, Desiatov B, Khurgin J, Shappir J, Levy U. Locally oxidized silicon surface-plasmon schottky detector for telecom regime. *Nano Lett* **11**, 2219–2224 (2011).
42. Knight M W, Sobhani H, Nordlander P, Halas N J. Photodetection with active optical antennas. *Science* **332**, 702–704 (2011).
43. Sobhani A, Knight M W, Wang Y M, Zheng B, King N S *et al.* Narrowband photodetection in the near-infrared with a plasmon-induced hot electron device. *Nat Commun* **4**, 1643 (2013).
44. Ho Y L, Huang L C, Delaunay J J. Spectrally selective photocapacitance modulation in plasmonic nanochannels for infrared imaging. *Nano Lett* **16**, 3094–3100 (2016).
45. Pankove J I. *Optical Processes in Semiconductors* (Dover, New York, 1971).
46. Loferski J J. Theoretical considerations governing the choice of the optimum semiconductor for photovoltaic solar energy conversion. *J Appl Phys* **27**, 777–784 (1956).
47. Taflove A, Hagness S C. Computational Electrodynamics: The Finite-Difference Time-Domain Method 3rd ed (Artech House, London, 2005).
48. Richard S, Aniel F, Fishman G. Energy-band structure of Ge, Si, and GaAs: A thirty-band $k{\cdot}p$ method. *Phys Rev B* **70**, 235204 (2004).
49. Maier S A. *Plasmonics: Fundamentals and Applications* (Springer, New York, 2007).
50. Koshida N, Koyama H. Visible electroluminescence from porous silicon. *Appl Phys Lett* **60**, 347–349 (1992).
51. Zheng J P, Jiao K L, Shen W P, Anderson W A, Kwok H S. Highly sensitive photodetector using porous silicon. *Appl Phys Lett* **61**, 459–461 (1992).
52. Yatsui T, Ohtsu M. Production of size-controlled Si nanocrystals using self-organized optical near-field chemical etching. *Appl Phys Lett* **95**, 043104 (2009).
53. Yatsui T, Nakahira Y, Nakamura Y, Morimoto T, Kato Y *et al.* Realization of red shift of absorption spectra using optical near-field effect. *Nanotechnology* **30**, 34LT02 (2019).
54. Iwasa T, Nobusada K. Nonuniform light-matter interaction theory for near-field-induced electron dynamics. *Phys Rev A* **80**, 043409 (2009).
55. Yamaguchi M, Nobusada K, Kawazoe T, Yatsui T. Two-photon absorption induced by electric field gradient of optical near-field and its application to photolithography. *Appl Phys Lett* **106**, 191103 (2015).
56. Yamaguchi M, Nobusada K, Yatsui T. Nonlinear optical response induced by a second-harmonic electric-field component concomitant with optical near-field excitation. *Phys Rev A* **92**, 043809 (2015).
57. Yamaguchi M, Nobusada K. Large hyperpolarizabilities of the second harmonic generation induced by nonuniform optical near fields. *J Phys Chem C* **120**, 23748–23755 (2016).
58. Fang C Z, Liu Y, Zhang Q F, Han G Q, Gao X *et al.* Germanium-tin alloys: applications for optoelectronics in mid-infrared spectra. *Opto-Electron Adv* **1**, 180004 (2018).
59. Lei S D, Ge L H, Najmaei S, George A, Kappera R *et al.* Evolution of the electronic band structure and efficient photo-detection in atomic layers of InSe. *ACS Nano* **8**, 1263–1272 (2014).
60. Li H, Han X, Pan D, Yan X, Wang H W *et al.* Bandgap engineering of inse single crystals through S substitution. *Cryst Growth Des* **18**, 2899–2904 (2018).
61. Hamer M J, Zultak J, Tyurnina A V, Zólyomi V, Terry D *et al.* Indirect to direct gap crossover in two-dimensional InSe revealed by angle-resolved photoemission spectroscopy. *ACS Nano* **13**, 2136–2142 (2019).
62. Wang X D, Wang P, Wang J L, Hu W D, Zhou X H *et al.* Ultrasensitive and broadband MoS_2 photodetector driven by ferroelectrics. *Adv Mater* **27**, 6575–6581 (2015).
63. Kufer D, Konstantatos G. Highly sensitive, encapsulated MoS_2 photodetector with gate controllable gain and speed. *Nano Lett* **15**, 7307–7313 (2015).
64. Tang L, Kocabas S E, Latif S, Okyay A K, Ly-Gagnon D S *et al.* Nanometre-scale germanium photodetector enhanced by a near-infrared dipole antenna. *Nat Photonics* **2**, 226–229 (2008).
65. Chen X P, Zhu H L, Cai J F. High-performance 4H-SiC-based ultraviolet *p-i-n* photodetector. *J Appl Phys* **102**, 024505 (2007).
66. Liao M Y, Wang X, Teraji T, Koizumi S, Koide Y. Light intensity dependence of photocurrent gain in single-crystal diamond detectors. *Phys Rev B* **81**, 033304 (2010).
67. Koizumi S, Watanabe K, Hasegawa M, Kanda H. Ultraviolet emission from a diamond pn junction. *Science* **292**, 1899–1901 (2001).
68. Camacho-Aguilera R E, Cai Y, Patel N, Bessette J T, Romagnoli M *et al.* An electrically pumped germanium laser. *Opt Express* **20**, 11316–11320 (2012).
69. Joshi R K, Shukla S, Saxena S, Lee G H, Sahajwalla V *et al.* Hydrogen generation *via* photoelectrochemical water splitting using chemically exfoliated MoS_2 layers. *AIP Adv* **6**, 015315 (2016).

Acknowledgements

The author wishes to express special thanks to Drs. Kenji Iida (Institute for Molecular Science), Masashi Noda (University of Tsukuba), Maiku Yamaguchi (University of Tokyo), Prof. Katsuyuki Nobusada (Institute for Molecular Science) and Kazuhiro Yabana (University of Tsukuba) for their active support and discussions. This work was partially supported by JSPS KAKENHI (Nos. JP18H01470, JP18H05157), a MEXT as a social and scientific priority issue (Creation of new functional devices and high-performance materials to support next-generation industries: CDMSI) to be tackled by using post-K computer (ID: hp170250), Asahi Glass Foundation, and Research Foundation for Opto-Science and Technology.

Competing interests

The author declares no competing financial interests.